PCCP

PAPER

View Article Online
View Journal | View Issue

Cite this: *Phys. Chem. Chem. Phys.*, 2019, **21**, 24702

Modified potential for atomistic simulation of the growth of carbon materials from binary alloy catalysts†

Jaewoong Hur

Received 15th July 2019,
Accepted 17th September 2019

DOI: 10.1039/c9cp03966j

rsc.li/pccp

A new hybrid bond order potential has been developed and implemented to describe carbon–bimetallic alloy interactions, which are involved in the catalytic growth of carbon materials such as graphene and carbon nanotubes on the surface of binary alloy catalysts. In carefully adjusting the parameters, the potential energy fitting correlated with the results calculated from the density functional theory (DFT) method leads to a high quality empirical force field with an average error of $<4.5\%$ only. With the PES accuracy, in total 16 (*n*,*m*) have been successfully obtained from the MD trajectories in this work, and the structural evolution including random chirality and diameter formation has been identified. The newly modified force field is expected to be useful for modelling the spontaneous growth of carbon materials, particularly tubes on binary alloy clusters, giving an idea of how these C–C, C–M, and M–M interactions affect the growth behavior of carbon nanotubes. In addition, the new FF is only valid for liquid alloy nanoparticles at this time, but the use of solid alloy nanocatalysts with the new FF can be further employed for 2-D material growth such as graphene layer growth.

Introduction

Carbon material formation processes that involve changes in bonding configurations can be simulated either by quantum mechanical methods or by classical potentials in treating bond formation or dissociation. A variety of interatomic potentials have widely been used for treating reactive systems classically,[1–7] and in those models, numerous chemical effects draw upon the strength of a pair and a many-body interaction induced by the chemical bonding environments of the bonds, but the specific implementations are different.

A force field (FF) of an elemental metal–carbon system has been developed previously by employing functions that only consider the use of a pure catalyst for modelling carbon–monometal interactions in catalyzed carbon and hydrocarbon materials.[4,7–12] However, to date, an effective force field that describes carbon–bimetallic alloy interactions, primarily for understanding the mechanism of growth of various carbon materials based on binary alloy catalysts, has not been developed yet. Thus, through a modification to the carbon–metal (C–M) potential using a pure metal catalyst,[7] the C–M potential can be extended and this is clearly valuable to explore the energetics of distinct bonding environments in carbon–bimetallic alloy systems and structural evolution characteristics taken from molecular dynamics (MD) trajectories.

A central development of the new hybrid bond order potential (BOP) is the capability to describe various bonding configurations, reflecting carbon growth derived from binary alloy catalysts, which all involve C–C, C–M (*i.e.*, C–M_{1st} and C–M_{2nd}), and M–M interactions. For C–C interactions, the reactive empirical bond order potential (REBO), which is one of the well-known Tersoff–Brenner style models, pioneered by Tersoff[1] and extended by Brenner,[2] including AIREBO developed by Stuart,[3] has been adopted. An additional term, α_D^{CM}, introduced by Martinez-Limia[9] has been included in the newly developed FF to account for the binary metal environment around a C–C bond, and hence the C–C bond strength surrounded by the coordinated binary metal can be reflected. Newly modified many-body potential functions using Morse-type attractive and repulsive terms for C–M_{1st} and C–M_{2nd} interactions, conceptually similar to a pure metal–carbon potential originally proposed by Maruyama[10] and partially extended by previous studies,[7–9] have been implemented. For binary M–M interactions, a long-range Finnis–Sinclair potential extended by Rafii-Tabar and Sutton[13] has been benchmarked, and newly implemented in the developed FF model by a slight modification of the functional terms.

In applying Pt and Cu metals as the binary alloy catalyst for the new potential, each of platinum and copper has been taken into account as an obviously important catalyst for diverse

Center for Multidimensional Carbon Materials (CMCM), Institute for Basic Science (IBS), Ulsan, 44919, Republic of Korea. E-mail: jwhur75@unist.ac.kr

† Electronic supplementary information (ESI) available: The potential functions, parameters, energetics, and MD simulation results of the new FF model and DFT calculation results. See DOI: 10.1039/c9cp03966j

catalytic reactions that is also used in the synthesis of carbon nanostructures. Moreover, Pt–C and Cu–C interatomic environments have been well described by analytical interatomic BOPs,[4,11] which are similar in form to the family of empirical BOPs. In this sense, carbon growth modelling using a Pt–Cu binary alloy catalyst, which can possibly be a fascinating candidate, is able to provide insight and to guide experimental studies using the new potential model in terms of analyzing the carbon growth process based on heterogenous catalysis, similarly to employing Cu–Ni and Pt–Au.[14]

This study is begun by briefly introducing the potential energy surface (PES) concept in the new hybrid BOP, and explaining a new modification of the C–M_{1st}/M_{2nd} potential functions that contribute to implementing the usage of a binary alloy catalyst in carbon growth simulations as well as the new implementation of M–M interaction terms for the alloy metals. These extensions allow one to have meaningful PES descriptions of carbon–bimetal bonding features and to simulate the evolutionary structure formation of nanocarbons such as single-walled carbon nanotubes (SWCNTs), particularly using Pt–Cu alloy liquid clusters in this work.

Model and methods

Carbon–metal potentials[7–10] have been developed to evaluate bonding interactions between pairs of interacting atoms *i* and *j* by summing repulsive and attractive potential terms with the relative bond strength regulated by a two-body and an *N*-body term. From this perspective, the accuracy of the new hybrid empirical bond order potential is essentially dependent on the good descriptions of the PES induced by any possible interactions, involved in bond forming and breaking processes of atoms *i* and *j*. And, the potential accuracy contributes to reliable MD simulations, especially in carbon material growth.

Potential energy surface (PES)

An empirical approach and implementation of the new concept using a binary alloy catalyst for carbon material growth were introduced to extend the form of the previous hybrid reactive potentials and to ensure the accurate PES of the target chemical bonding environments in this work,

$$E^{TOT} = E^{CM} + E^{CC} + E^{MM} \quad (1)$$

where E^{CM}, E^{CC}, and E^{MM} are carbon–metal, carbon–carbon, and metal–metal interaction energy terms. The interactions described by the new hybrid BOP are categorized into three sections: (a) C–M_{1st} and C–M_{2nd} interactions between carbon and the bimetallic alloy, named M_{1st} and M_{2nd} for each of the binary alloy metals, which is indeed Pt or Cu herein, (b) C–C interactions taking place at the metal coordination around the C–C bonds, and (c) M–M interactions of the bimetallic alloy.

(a) New modification for the C–M_{1st} and C–M_{2nd} interactions. Many-body potential functions that are treated with Morse-type repulsive and attractive potential terms were previously used in the C–Ni potential,[7–9]

$$E^{CM} = \sum_i \sum_{j>i} E_{ij}^{CM} \quad (2)$$

A key modification in the development of the new hybrid BOP is here that the *N*-body potential functions are newly designed and further implemented for C–M_{1st} and C–M_{2nd} interactions between carbons and binary alloy metals,

$$E^{CM} = \sum_i \sum_{j>i} E_{ij}^{CM_{1st}} + \sum_i \sum_{j>i} E_{ij}^{CM_{2nd}} = \sum_i \sum_{j>i} E_{ij}^{C(M_{1st}+M_{2nd})} \quad (3)$$

where M = M_{1st} + M_{2nd}. The potential terms related to the new modification can be found in detail elsewhere (ESI†). Apparent bonding configurations between small carbons including a few tubes and the Pt–Cu alloy catalyst have been considered to define the bonding characteristics necessary for an accurate PES against a DFT energy pattern and tube growth in MD simulations. The PES characteristics are obtained from the energy-minimized geometries of the C–M_{1st} and C–M_{2nd} bonding configurations between selected carbon materials and the Pt–Cu catalyst, using new parameterization and reparameterization. Further validations of the newly modified FF model to provide a more chemically and physically appropriate representation of the underlying bonding effects in the target system were conducted by using the distinct bonding structures of C_1 and the tubes with a pure Pt or Cu metal catalyst, including each of their own parameterizations respectively.

(b) Counting metal coordination around C–C bonds by the new modification. Typical short-range bonding structures leading to the strength of any covalent bonding interactions are taken into account by the class of BOP models. Bond length, bond angle, coordination numbers, and conjugation effects all have a part in the bond strength of any particular atomic interactions in the BOP models. In addition, the C–M interactions around a C–C bond environment are accounted for, because the bond order is also affected by the atomic coordination number of metal nanoparticles. Obviously, a C–C bond with many metal neighbors becomes weaker than a C–C bond with few metal neighbors. In counting the metal coordination surrounding a C–C bond, the effects of the Pt–Cu alloy metals are considered in the newly fitted potential to evaluate the C–C bond strength modulated by the local environments of the bimetallic alloy catalyst.

(c) New implementation of M–M interactions using a binary alloy catalyst. In the new FF model, the extended Finnis–Sinclair (FS) potential studied for bimetallic f.c.c. alloys[13] was benchmarked to describe binary M–M interactions as having the new implementation with a simple mathematical change and parameterization (more details in the ESI†). In the M–M interaction term, long-range pair interactions and many-body unsaturated covalent bonding interactions at short range are both described. Since the alloy metal catalyst used in this work is bimetallic, the M–M interactions represent M_{1st}–M_{1st}, M_{1st}–M_{2nd}, and M_{2nd}–M_{2nd} interactions, which determine the energetics of $Pt_3Cu(111)$, as calculated by the new FF model and compared to their DFT energy characteristics.

MD set-up and defect healing algorithm

Atomistic MD simulations of the new hybrid BOP have been performed by using random carbon injections into the Pt–Cu alloy catalyst at target temperatures between 1250 and 1310 K,

which are close to the range of temperature that is used for chemical vapor deposition synthesis, between 800 and 1300 K.[7–9,11,15] In the meantime, the atomic velocities at the lower simulation temperatures are relatively reduced, which more likely causes an inefficient healing process during the tube growth at the tip of the tubes interfaced with the Pt–Cu alloy catalyst, thus affecting the quality of the nanotubes. All simulations of the carbon material growth based on mainly $Pt_{27}Cu_{27}$ and $Pt_{28}Cu_{28}$ take each MD step running for the time period between 28 ps and 42 ps. Each of the binary alloy catalysts (*i.e.*, $Pt_{27}Cu_{27}$ and $Pt_{28}Cu_{28}$) is placed in a periodic box of unit volume to run the MD simulation starting from carbon nucleation, C_{24}, the hemisphere of a fullerene group, and the closed tube caps as a precursor. In the MD simulations, the equations of motion are integrated with the velocity Verlet algorithm using a time step of 0.5 fs, and the temperature is controlled by velocity rescaling using the Berendsen thermostat.

The addition of one carbon atom to the Pt–Cu metal cluster is completed for every MD step, and after adding 40 carbons, the topological defect healing algorithm begins to use the Stone–Wales (SW) transformation[16] and Metropolis–Hastings algorithm.[17] In the SW transformation, the random rotation of an irregular sp^2 hybridized C–C bond by 90° around the $C–M_{1st}/M_{2nd}$ environment takes place, and thus the local structural configuration becomes changed to locate the local energy minimum by performing jumps into another basin. During this process, it is determined by the Metropolis method whether or not the new local energy minimum is acceptable, and the probability is expressed as

$$\begin{aligned} P &= 1, \text{ if } \Delta E \leq 0 \\ P &= e^{-\frac{\Delta E}{k_B T}}, \text{ if } \Delta E > 0 \end{aligned} \quad (4)$$

where k_B is the Boltzmann constant, T is the target temperature, and ΔE is the energy difference between the previous and current relaxed configurations during the local structure optimization.

Chirality determination

The atomic structural configurations of the nanotubes can be distinguished by the chirality, defined by the chiral vector $\vec{C}_h$ and the chiral angle θ. The chiral vector can be expressed by using the lattice translational indices (n,m) and the unit vectors $\vec{a}_1$ and $\vec{a}_2$,

$$\vec{C}_h = n\vec{a}_1 + m\vec{a}_2 \quad (5)$$

where (n,m) use integers indicating the number of hexagons along with the zig-zag type of carbon π-bonds in the hexagonal lattice. The chiral angle θ is defined as the angle between the vectors $\vec{C}_h$ and $\vec{a}_1$ in the range of $0° \leq |\theta| \leq 30°$,

$$\theta = \tan^{-1}\frac{\sqrt{3}m}{2n+m}. \quad (6)$$

Eqn (6) is one of three equations that can describe the chiral angle. Within the 0°–30° range, the chiral angle of (n,m) is equivalent to that of (m,n).

Results and discussion

Potential energy surface using the Pt–Cu alloy catalyst

Since the new hybrid BOP is able to provide a more rich means of describing carbon material growth based on the Pt–Cu alloy catalyst, discrete types of carbon materials need to be used for more accurate PES descriptions. The carbon materials used here are the following: C_1 having different bonding positions with binary metal crystal structures as the PES fitting data set and a dimer, a chain, C_{20}, C_{21}, $C_{24}(D_{6h})$, and $C_{24}(C_s)$ providing distinct bonding configurations with the bimetal surfaces as the PES validation data set.

Fig. 1 shows a bond formation energy trend that was evaluated at the energy-minimized geometries containing $C–M_{1st}$ and $C–M_{2nd}$ bonds comprised of the discrete bonding configurations between C_1 and the Pt_3Cu alloy catalyst, as calculated with the new FF model and new parameters, against the DFT energy trend. With modification and parameterization, the regression curve (R^2 = 0.963), correlated with the bond formation energy pattern of C_1 binding to the Pt–Cu alloy calculated by the new FF model, presents a very similar slope to that (R^2 = 0.967) of the DFT bond formation energy pattern. The parameter-fitted regression curve slope more likely contributes a reliable extrapolation based on the DFT energetics for more bonding configurations between carbons and the Pt–Cu catalyst. With this slope, the average percent error of three different types of bonding configurations is 4.26%, representing a root mean square (RMS) average difference between the new FF and DFT energies of <0.27 eV between ~ -5 eV and ~ -7 eV (an average bond energy per bond of ~ -2.1 eV for both the new FF and DFT energies).

In the validation data set, only a $<3.8\%$ average percent error of six different types of carbon materials which are geometry-optimized on the Pt–Cu metal surface is shown, and the six different carbons reveal dominant bonding characteristics for carbon material growth. Shown in Fig. 2, the average RMS difference between the new FF and DFT energies for the six

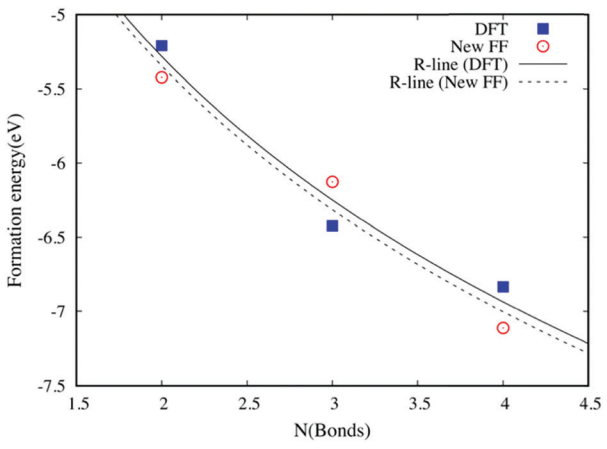

Fig. 1 A bond formation energy pattern of the C_1 bonding configurations based on the Pt_3Cu bimetallic alloy catalyst in the fitting data set, as calculated with the new force field, compared to a DFT energy pattern showing nonlinear regression.

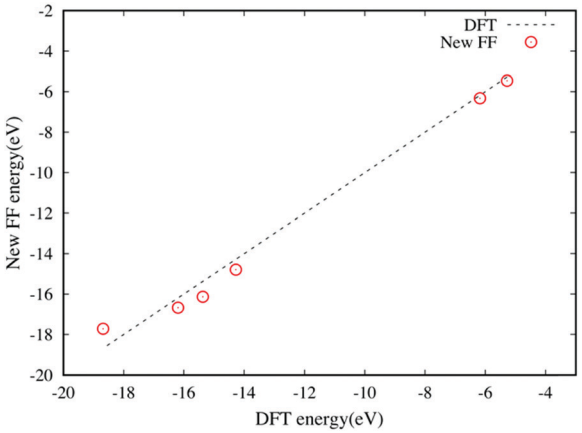

Fig. 2 A bond formation energy pattern of distinct bonding configurations, obtained from minimum energy geometries, between a dimer, a chain, C_{20}, C_{21}, $C_{24}(D_{6h})$, and $C_{24}(C_s)$ and the Pt_3Cu alloy catalyst in the validation data set, as calculated with the new force field, against DFT energies.

different carbons shows <0.59 eV between ~ -5 eV and ~ -19 eV, which indicates a relatively more accurate energy fitting than that of the previous works.[7,21] In this sense, it is shown that the new FF energies are well correlated with the DFT energies (correlation coefficient R^2 = 0.988). The bond formation energy values calculated with the minimum energy geometries for the different carbon species summarized in Table S3 are included in the ESI.†

PES using the new implementation for binary M–M interactions

The nature of the M–M interactions is essential to consider by modelling two-body and *N*-body potential terms, and the new hybrid BOP contains binary M–M interaction terms that are slightly reformulated to use with liquid Pt–Cu alloy clusters, based on the energetics of the f.c.c. Pt–Cu(111) alloy system. The bond formation energies with geometry-optimized structures (*i.e.*, 4×4, 6×6, and 8×8 unit cells) are between -4.86 eV per atom and -4.93 eV per atom as estimated by both the new FF and DFT calculations. The RMS errors of the systems are 0.81 meV per atom, 23.85 meV per atom, and 69.18 meV per atom respectively, showing that the average percent error of the three different unit cell f.c.c. structures is only 0.64%. Thus, the new FF energy fittings using 17 appropriate parameters are well consistent with the DFT energy fittings (see the ESI† for details).

Validation of the modified FF by employing elemental catalysts

In order to ensure that the new FF model has not been overfit to the training data set and validation data set employing various bonding configurations between the carbon materials and the Pt–Cu alloy catalyst, at this time, a pure catalyst (*i.e.*, each of Pt and Cu metals) for bond formation energy evaluation is applied with reparameterization.

In estimating bond formation energies at the energy-minimized geometries of C_1 and selected (4,4) and (7,0) tubes connected to a pure Pt catalyst, an average C_1–Pt_n (*n*: 1–4) energy per bond of ~ -3.2 eV is shown for both the new FF and DFT energies. From the point of view of percent error, the average percent error of the C_1–Pt_n (*n*: 1–4) energy fittings is 7.42%, in which the percent errors of the energy fittings for the C_1–Pt_1 and C_1–Pt_2 bonding structures become slightly higher when adjusting the parameters to fit the regression curves correlated with the new FF (R^2 = 0.831) and DFT (R^2 = 0.994) bond formation energy patterns. Nonetheless, fitting the regression curve slopes produced by the C_1–Pt_n (*n*: 1–4) bond formation energy patterns is more importantly considered for more C_x–Pt_y (*x*: >1 and *y*: >5) bonding environments. From this consideration, $<0.45\%$ errors of the energy fittings for both (4,4) and (7,0) tubes on the Pt metal surface are obtained, and the RMS errors of the C–Pt bond formation energies for the two tubes are both <0.15 eV.

Likewise, in the bond formation energy evaluations of C_1 and the chosen (3,3) and (5,0) tubes binding to the pure Cu catalyst, ~ -2.5 eV as an average energy per bond by the newly modified FF and DFT calculations is calculated with reparameterization. Unlike C_1–Pt_n (*n*: 1–4), the average percent error of C_1–Cu_n (*n*: 1–4) is 4.49%, which includes the consistent regression curve slope correlated with the new FF (R^2 = 0.958) energy pattern in line with the slope of the DFT (R^2 = 0.991) energy trend. In addition, $<0.95\%$ errors of the energy fittings for two targeted (3,3) and (5,0) tubes are achieved, indicating that the RMS errors of the C–Cu bond formation energies for the two tubes are both <0.22 eV. Therefore, it is shown that the energy fitting results from the new FF model are consistent with the DFT energies just like the results of the C–Pt bonding configurations.

Hexagon formation in (*n*,*m*) growth

The atomic scale simulation process of 1-D tube growth is a crucial part in understanding and predicting the spontaneous tube hexagon formations occurring at the Pt–Cu alloy surface. A local minimum structure optimization determined from the basin-hopping algorithm is carried out by random structure relaxation and SW transformation, as mentioned earlier. For specific descriptions of the hexagon formation process displayed in Fig. 3, six steps (*i.e.*, step (a)–step (f)) of (5,5) growth are employed to explain how a new hexagon at a specific area (*i.e.*, mainly at the edge) of the tube around a liquid $Pt_{27}Cu_{27}$ alloy cluster is formed.

An opened hexagon with a dangling carbon bond on the edge of (5,5) forms a closed 6-membered ring by separate C atom addition, shown in between steps (a) and (b). After one hexagon is formed, the dangling bond is connected to the tip of an armchair-like site of (5,5) to form a pentagon in step (c). In step (d), a new C atom flowing around the alloy catalyst is added to the edge of a neighboring armchair-like site of the pentagon already formed in step (c) to make a new dangling bond. With this dangling bond and a new additional C atom, a heptagon coupled to the pentagon is newly formed in step (e). The C–C bond created at the bottom of the heptagon is rotated by 90°, and hence two hexagons are generated in step (f). The formation process of a new hexagon at an armchair-like site is consistent with the prediction from DFT calculations.[18]

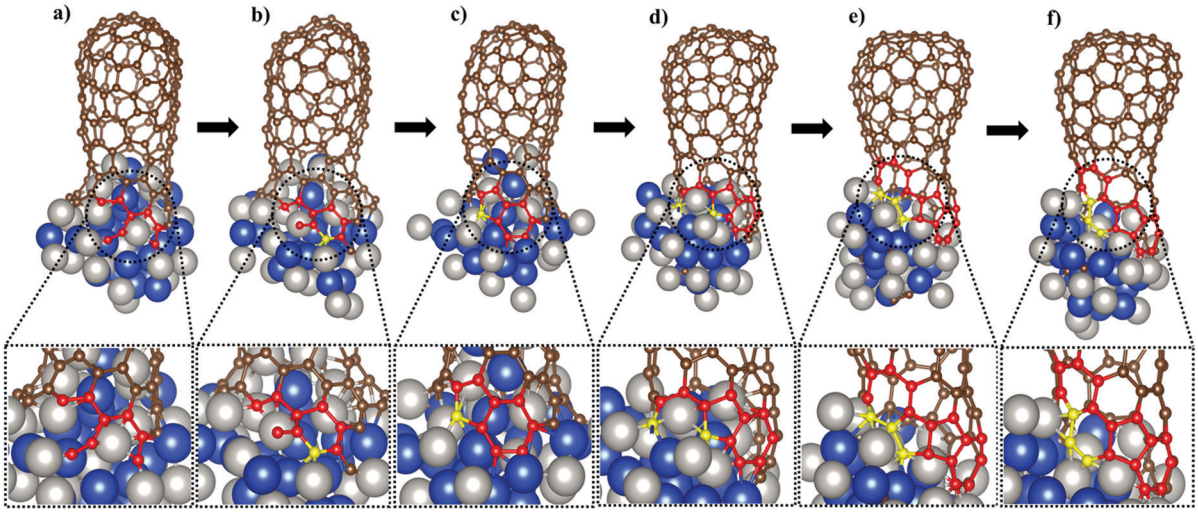

Fig. 3 The atomistic simulation snapshots of hexagon formations in the (5,5) tube growth process using a liquid $Pt_{27}Cu_{27}$ alloy cluster from step (a) through step (f). The gray and dark blue-colored balls represent Pt and Cu metals, respectively. The brown-colored balls represent C atoms in (5,5), where the red-colored balls are displayed for the local structural transformations around C–C bonds, and the yellow-colored balls as C atoms indicate the specific positions for hexagon formation.

(*n*,*m*) growth from various carbon precursors

(*n*,*m*) growth from the Pt–Cu alloy catalyst modelled by the new hybrid BOP can be observed in MD simulations as microscopic scaled simulations. Fig. 4 illustrates the structural evolution of the carbon domain up to being a little longer (4,4) tube, defined by the chiral vector and angle, based on the Pt_{28}–Cu_{28} alloy catalyst by conducting continuous carbon additions.

In the case of (4,4), the tube growth starts from carbon nucleation (*i.e.*, a carbon seed), and a few carbons flowing around the Pt_{28}–Cu_{28} alloy catalyst are seen in the snapshot (stage (a)) taken from the MD trajectory at 1.29 ns of the time period. In stage (b), a chain is formed at 3.56 ns, and a first sp^2-bonded hexagon is generated at 3.74 ns, appearing in stage (c). The formation of a curved graphitic layer containing a few hexagons and pentagons on the Pt_{28}–Cu_{28} metal surface takes place at 4.24 ns, presented in stage (d). It is known that an ideal stable cap, consisting of pentagons and hexagons only, should have six pentagons to be stable following Euler's rule,[19] and the distribution of the six pentagons over the cap might determine the diameter and chirality of the tube grown.[8] However, in a more realistic sense, it might be assumed that six pentagons do not necessarily evenly distribute over the tube cap associated with the presence of other hexagons. In other words, two pentagons are possibly connected to one another in a partial area of the cap with curvature during the cap formation, shown in stage (e), and this can be linked to the narrower diameter and chirality determinations.

In terms of the grown tube seen in stage (f) of the 5.32 ns snapshot, a short tube newly appears, and becomes longer with continuous C atom additions to the interface between the tube edge and the Pt_{28}–Cu_{28} alloy cluster as displayed in stage (g). The further grown tube presented in stage (h) is formed at 6.94 ns, and this (4,4) tube, being relatively longer, contains ten pentagons, thirty three hexagons, and five heptagons. The number of polygons indicates that the great number of hexagons (at least three times larger) involved in the (4,4) matrix contributes to maintaining a more 1-D like tube shape, unlike the other polygons causing tube curvature.

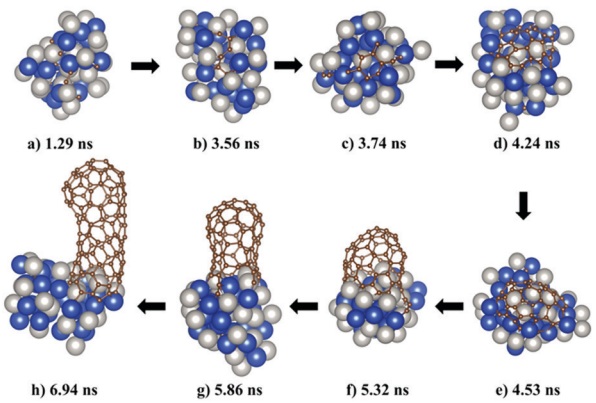

Fig. 4 Structural evolution snapshots (stage (a)–(h)) taken from MD trajectories in terms of the (4,4) tube growth based on the Pt_{28}–Cu_{28} binary alloy catalyst. The gray, dark blue, and brown-colored balls indicate Pt, Cu, and C atoms, respectively.

Diameter and chiral selectivity

While forming pentagons, hexagons, and heptagons, which are the main polygons that contribute to the simulated (*n*,*m*), the chirality and diameter of the tubes are spontaneously determined during the tube growth. In simulating the tube growth based on only Pt_{27}–Cu_{27} and Pt_{28}–Cu_{28} alloy catalysts, most tube chirality, as shown in Fig. 5, with different diameters, has been indiscriminately generated: from (4,4) with a ~5.65 Å diameter to (8,3) with a ~7.68 Å diameter, which are all approximate diameters due to their curvature. This tube chirality pattern, corresponding to the bimetallic alloy composition (*i.e.*, 1 : 1 ratio

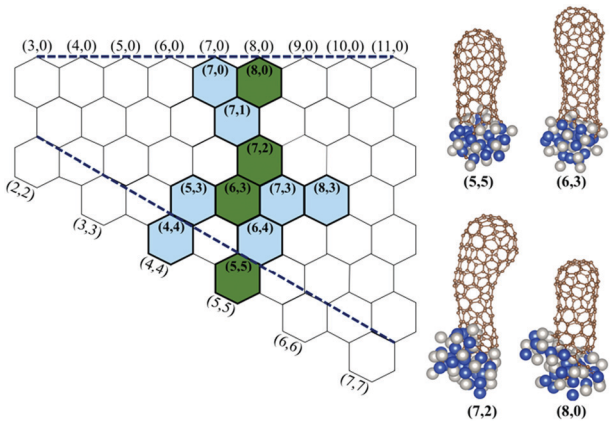

Fig. 5 Chirality distribution of the grown tubes using the Pt–Cu alloy nanoparticles, as defined by the chiral vector $\left(\vec{C}_h\right)$ and angle (θ). The chiral indices mapped for the simulated tubes are presented: the green chiral indices indicating more than two simulated tubes and the light-blue chiral indices representing a simulated tube. The gray, dark blue, and brown-colored balls indicate Pt, Cu, and C atoms, respectively.

of a Pt–Cu alloy liquid cluster in this work) and number of Pt–Cu alloy nanoparticles, is somewhat different from the tube chirality that stems from each pure Pt and Cu catalyst (refer to the ESI†). Larger diameters of the tubes have been obtained from the tube growth process using Cu_{54}, as compared to using the Pt_{27}–Cu_{27} alloy catalyst, related to the catalyst cluster size, even though Cu_{54} has a smaller cluster size than that of the Pt_{27}–Cu_{27} metal cluster. In this sense, it is found that the tube diameter determined by the Pt–Cu alloy catalyst becomes relatively smaller than that of the tube derived from an elemental catalyst.

Conclusions

A new hybrid bond order potential to model the C–M_{1st} and C–M_{2nd} interactions for carbon material growth in response to adopting bimetallic alloy catalysts has been developed. The simulation results show a consistent PES with acceptable percent errors against DFT energies in both the training set and the validation set, which have distinct bonding configurations between carbons and the Pt–Cu alloy catalyst.

Implementation and fitting, including parameterizations, of the new C–M_{1st} and C–M_{2nd} interaction function produce only $<4.5\%$ energy errors. Another reliable estimate of the expected average percent error (*i.e.*, $<3.8\%$) was obtained from validation against a set of carbons such as a dimer, a chain, C_{20}, C_{21}, $C_{24}(D_{6h})$ and $C_{24}(C_s)$ that were not used in the fitting set. In the meantime, additional validation of the new algorithm for the C–M_{1st} and C–M_{2nd} interaction term was carried out by calculating the energetics of C_1 and selected (n,n) and (n,0) binding to an elemental catalyst (*i.e.*, Pt or Cu). From the calculation, the regression curve fitting between the new hybrid FF and DFT energy patterns for more C_x–M_y (M: Pt or Cu, x: >1, and y: >5) bonding configurations gives $<0.95\%$ energy errors for the tested tubes on an elemental Pt or Cu metal surface. The new implementation of M–M interactions with a simple modification, benchmarked for the Pt–Cu surface, provides RMS errors of 0.81 meV per atom, 23.85 meV per atom, and 69.18 meV per atom for 4×4, 6×6, and 8×8 unit cells of the Pt–Cu surface respectively, showing that the average percent error per atom of the three different unit cell fcc structures is only 0.64%.

The new hybrid FF model uses more parameters than the C–Ni potential[7–9] (9 more parameters for the C–M_{1st}/M_{2nd} interaction term and 12 more parameters for the M–M interaction term). This is not surprising because in comparison to the C–Ni potential, the C–M_{2nd} term and the M_{1st}–M_{2nd} and M_{2nd}–M_{2nd} terms in the new hybrid FF model are necessarily implemented to describe many-body interactions between carbons and bimetallic alloy catalysts. In that sense, the computational time expense required for an energy estimation increases by an average of 3.8% for C_1 (*i.e.* bridge, hollow, and bulk sites) and 13.1% for C_{20}, C_{21}, and C_{24} binding to the Pt–Cu catalyst, and it is quite natural due to more terms and parameters. Nonetheless, it is probable that a carefully optimized code would be able to calculate the new potential function with minimized expense. Despite more interaction terms being implemented in the modified FF, the PES accuracy is reasonable, and thus it can be expected that the energies of nanocarbons based on binary alloy catalysts (other metal combinations like Cu–Ni, W–Co *etc.*[14,20] with their own parameterizations) are well correlated with the quantum mechanical energies.

MD simulations of (n,m) growth starting from carbon nucleation, 2-D C_{24}, a group of fullerenes such as C_{80}, C_{90}, and C_{100} used as hemisphere-like, and closed tube caps are employed to model a catalytic synthesis process of tubes from the Pt–Cu metal alloy. The apparent bonding characteristics of the carbon precursors interacting with the Pt–Cu catalyst are observed in the structural evolution of a local minimum structure during the atomistic simulation process. As samples simulated in this work, a total of 16 grown tubes that are identified from (4,4) to (8,3) have successfully been obtained from the MD simulations as well as 5 other (n,m) with an elemental catalyst (Pt or Cu). An interesting pattern of the tube diameter from the Pt–Cu alloy catalyst is that random chirality distributions with narrower diameters have been formed, compared to the tubes grown from a pure Cu catalyst that even has a smaller cluster size.

The current implementation serves as a proof of concept, demonstrating the value of the newly modified FF for carbon material growth using a binary alloy catalyst, and thus more carbon material growth with other bimetallic catalysts (*e.g.*, Cu–Ni, Pt–Au, and W–Co *etc.*) could likewise benefit from the new functional terms in the new FF model. In addition, even though Pt–Cu liquid nanocatalysts are only used in the new FF using random distributions of the nanoparticles at this time, solid alloy catalysts could be further used for 2-dimensional material growth such as graphene layer growth.

Conflicts of interest

There are no conflicts to declare.

Acknowledgements

The author gratefully acknowledges the support from the Institute for Basic Science (IBS-R019-D1), and this work was performed using the computational resources of IBS-CMCM. The author also thanks Feng Ding and Tianying Yan for sharing their potential code and discussion for IBS research work.

References

1 J. Tersoff, *Phys. Rev. B: Condens. Matter Mater. Phys.*, 1988, **37**, 6991.
2 D. W. Brenner, O. A. Shenderova, J. A. Harrison, S. J. Stuart, B. Ni and S. Sinnott, *J. Phys.: Condens. Matter*, 2002, **14**, 783.
3 S. J. Stuart, A. B. Tutein and J. A. Harrison, *J. Chem. Phys.*, 2000, **112**, 6472.
4 K. Albe, K. Nordlund and R. S. Averback, *Phys. Rev. B: Condens. Matter Mater. Phys.*, 2002, **65**, 195124.
5 A. C. T. van Duin, S. Dasgupta, F. Lorant and W. A. Goddard, *J. Phys. Chem. A*, 2001, **105**, 9396.
6 C. J. O'Brien, C. M. Barr, P. M. Price, K. Hattar and S. M. Foiles, *J. Mater. Sci.*, 2018, **53**, 2911.
7 Z. Xu, T. Yan and F. Ding, *Chem. Sci.*, 2015, **6**, 4704.
8 J. Zhao, A. Martinez-Limia and P. B. Balbuena, *Nanotechnology*, 2005, **16**, S575.
9 A. Martinez-Limia, J. Zhao and P. B. Balbuena, *J. Mol. Model.*, 2007, **13**, 595.
10 Y. Yamaguchi and S. Maruyama, *Eur. Phys. J. D*, 1999, **9**, 385.
11 X. W. Zhou, D. K. Ward and M. E. Foster, *J. Comput. Chem.*, 2015, **36**, 1719.
12 J. E. Mueller, A. C. T. van Duin and W. A. Goddard, *J. Phys. Chem. C*, 2010, **114**, 4939.
13 H. Rafii-Tabar and A. P. Sutton, *Philos. Mag. Lett.*, 1991, **63**, 217.
14 S.-P. Huang, D. S. Mainardi and P. B. Balbuena, *Surf. Sci.*, 2003, **545**, 163.
15 J. E. Herrera and D. E. Resasco, *J. Phys. Chem. B*, 2003, **107**, 3738.
16 A. J. Stone and D. J. Wales, *Chem. Phys. Lett.*, 1986, **128**, 501.
17 D. J. Wales and J. P. K. Doye, *J. Phys. Chem. A*, 1997, **101**, 5111.
18 Q. Yuan, Z. Xu, B. I. Yakobson and F. Ding, *Phys. Rev. Lett.*, 2012, **108**, 245505.
19 S. Iijima, *Mater. Sci. Eng., B*, 1993, **19**, 172.
20 F. Yang, X. Wang, D. Zhang, J. Yang, D. Luo, Z. Xu, J. Wei, J. Q. Wang, Z. Xu, F. Peng, X. Li, R. Li, Y. Li, M. Li, X. Bai, F. Ding and Y. Li, *Nature*, 2014, **510**, 522.
21 J. Hur and S. J. Stuart, *J. Chem. Phys.*, 2012, **137**, 054102.

